ORIGINAL PAPER

Nano-composites SnO(VO$_x$) as anodes for lithium ion batteries

B. Das · M. V. Reddy · G. V. Subba Rao ·
B. V. R. Chowdari

Abstract Nano-composites of SnO(V$_2$O$_3$)$_x$ (x=0, 0.25, and 0.5) and SnO(VO)$_{0.5}$ are prepared from SnO and V$_2$O$_3$/VO by high-energy ball milling (HEB) and are characterized by X-ray diffraction (XRD), scanning electron microscopy, and high-resolution transmission electron microscopy techniques. Interestingly, SnO and SnO(VO)$_{0.5}$ are unstable to HEB and disproportionate to Sn and SnO$_2$, whereas HEB of SnO(V$_2$O$_3$)$_x$ gives rise to SnO$_2$.VO$_x$. Galvanostatic cycling of the phases is carried out at 60 mAg^{-1} (0.12 C) in the voltage range 0.005–0.8 V vs. Li. The nano-SnO (V$_2$O$_3$)$_{0.5}$ showed a first-charge capacity of 435($\pm$5)mAh g^{-1} which stabilized to 380($\pm$5)mAhg^{-1} with no noticeable fading in the range of 10–60 cycles. Under similar cycling conditions, nano-SnO (x=0), nano-SnO(V$_2$O$_3$)$_{0.25}$, and nano-SnO(VO)$_{0.5}$ showed initial reversible capacities between 630 and 390($\pm$5)mAhg^{-1}. Between 10 and 50 cycles, nano-SnO showed a capacity fade as high as 59%, whereas the above two VO$_x$-containing composites showed capacity fade ranging from 10% to 28%. In all the nano-composites, the average discharge potential is 0.2–0.3 V and average charge potential is 0.5–0.6 V vs. Li, and the coulombic efficiency is 96–98% after 10 cycles. The observed galvanostatic cycling, cyclic voltammetry, and ex situ XRD data are interpreted in terms of the alloying–de-alloying reaction of Sn in the nano-composite "Sn-VO$_x$-Li$_2$O" with VO$_x$ acting as an electronically conducting matrix.

Dedicated to Prof. R. Schöllhorn on his 75th birthday.

B. Das · M. V. Reddy · G. V. Subba Rao · B. V. R. Chowdari (✉)
Department of Physics, National University of Singapore,
Singapore 117 542, Singapore
e-mail: phychowd@nus.edu.sg

Introduction

Lithium ion rechargeable batteries (LIBs) are the promising DC energy source for portable electronic devices. To satisfy the ever-increasing demand for high-energy density LIBs for applications in electric and hybrid electric vehicles and off-peak energy storage, lot of research effort is expended to find electrode materials, especially the anodes (negative electrodes) which possess high capacity and excellent cyclability [1–4]. Li alloy-forming elements M (M = Sn, Si, Sb) [1–8] have received much attention due to their ability of reversibly reacting with large amount of Li per formula unit. Among these, Si and Sn are considered as most promising elements, as they form alloys, Li$_{4.4}$M. Sn-based intermetallics, oxides, and composites are well studied as possible alternatives to graphite anode presently employed in the LIBs. However, almost all of them suffer from poor cycling performance due to the large unit cell volume variation (~300%), which causes disintegration of the electrode material during long-term charge/discharge process. The capacity fading can be suppressed to some extent by (a) incorporating suitable "matrix" elements, (b) reducing the particle size to nano-meter scale, and (c) choosing a suitable voltage range of cycling. Accordingly, nano-structured materials are explored as potential candidate anodes for LIBs because they can show large reversible capacities due to high surface area, high current rate capability due to short Li-ion diffusion path length, and minimization of the strain caused due to large volume variations during charge/discharge process [5].

Sn-based binary and ternary oxides in nano-form such as SnO [9], SnO_2 [10, 11], $CaO.SnO_2$ [12], and $CoSnO_3$ [13] have been studied as anode materials. The advantage of using oxides is that they can be synthesized with varying morphology, and particle and crystallite size can be manipulated in comparison to Sn metal. However, an obvious disadvantage is that the binary/ternary oxide is first reduced to Sn metal by Li, and only then the Li–Sn alloy formation can take place. Hence, a large irreversible capacity loss (ICL) occurs during the first-discharge–charge process. Among all Sn-based oxides, SnO is attractive because it has a theoretical capacity as high as 875 $mAhg^{-1}$ and will have a lower ICL compared to other Sn oxides. There are a few reports on the Li cyclability of bulk (micron size) and nano-SnO in the literature. Courtney and Dahn [14] found that bulk SnO can give an initial reversible capacity of 825 $mAhg^{-1}$, but the capacity fades drastically on long-term cycling in the voltage range 0.0–1.3 V vs. Li. But when the voltage range is restricted to 0.4–1.3 V, somewhat stable capacity is obtained up to 10 cycles. Li et al. [15] reported that the Li-cycling properties of SnO were influenced by the particle size, as was clear from studies on ball-milled SnO. Un-milled SnO gave a first-charge capacity as high as 760 $mAhg^{-1}$, but capacity fading occurred giving only 420 $mAhg^{-1}$ at the end of 11th cycle. Similar was the case with ball-milled SnO. Uchiyama et al. [16] reported a comparative Li cyclability study of SnO of different morphologies with that of commercial SnO. They found that both meshed and flat plate SnO showed initial capacities of 760 and 880 $mAhg^{-1}$, respectively, as compared to 525 $mAhg^{-1}$ for commercial SnO in the voltage range 0.1–1.0 V at 100 mAg^{-1}. However, drastic capacity fading was noticed in all cases after 20 cycles. Wang et al. [17] studied Li cycling of SnO and $Sn.Li_2O$ composite prepared by ball milling of SnO and Li metal. They noticed lesser ICL in the case of composite and better capacity retention when cycled in the voltage range 0.02–1.5 V at 0.1 $mAcm^{-2}$. The composite electrode showed 170 $mAhg^{-1}$ at the 100th cycle whereas ball-milled SnO showed only 20 $mAhg^{-1}$. Yang et al. [18] studied the Li cycling of SnO particles of different sizes in the voltage window 0.1–1.3 V and found an initial capacity of 530 $mAhg^{-1}$ at 0.4 $mAcm^{-2}$. Fairly high ICL was noted for fine particle SnO and a comparatively better capacity retention till 50 cycles (~350 $mAhg^{-1}$). Ning et al. [19] studied the Li cycling of nano-flower SnO in the voltage range of 0.01–2.0 V at 0.1 C rate. A fourth cycle charge capacity of ~750 $mAhg^{-1}$ was noticed, but the capacity faded to 450 $mAhg^{-1}$ within 20 cycles. Chen et al. [20] reported the cycling behavior of SnO carbon nano-tube nano-composite and observed a first-charge capacity of ~780 $mAhg^{-1}$ in the voltage range 0–2.0 V at

40 mAg^{-1}. However, capacity fading was noticed within 10 cycles, giving ~450 $mAhg^{-1}$. From the above discussion, it is clear that pure SnO in micron/nano-size and with various morphologies is prone to significant capacity fading on cycling. Composites with SnO appear to show some promise, even though not many studies are reported.

Recently, Reddy et al. [21] and Reddy et al. (submitted for publication) studied the Li-cycling properties of $VSbO_4$ and $(V_{1/2}Sb_{1/2}Sn)O_4$ and found that the presence of vanadium oxide (VO_x) in the composite can act as a good matrix and helps in suppressing the capacity fading of Sb and Sn oxide upon long-term cycling. It appears that the strain due to large volume variations caused by alloying–de-alloying reactions of Li_3Sb and $Li_{4.4}Sn$ is highly buffered due to the presence of VO_x. Recently, Park et al. [22] prepared the composite SnO.Ti.C by ball milling to yield $nano-Sn.TiO_2.C$ and examined its Li cyclability. When cycled in the voltage range 0–2.5 V vs. Li at 100 mAg^{-1}, an initial reversible capacity of ~750 $mAhg^{-1}$ was observed which slowly degraded to ~610 $mAhg^{-1}$ over 100 cycles (~18% capacity fading).

In the present study, we examined the Li-cycling behavior of the nano-composites SnO, $SnO(V_2O_3)_x$ (x=0.25, 0.5), and $SnO(VO)_{0.5}$ prepared by high-energy ball milling (HEB). It is known that V_2O_3 and VO exhibit metallic-type electronic conductivity at ambient temperature [23–25]. Studies by Reddy et al. [21] and Reddy et al. (submitted for publication) and our unpublished results have shown that pure V_2O_3 and VO_x (x≤1) do not show any significant Li-cycling behavior in the voltage range 0.005–1.0 V vs. Li. Thus, it can be concluded that the nano-composites $SnO(VO_x)$ are comprised of only one electrochemically active element (Sn) toward Li. Accordingly, the present results show that the nano-composite $SnO(V_2O_3)_{0.5}$ exhibits a reversible capacity of 380($\pm$5)$mAhg^{-1}$ with no noticeable capacity fading in the range 10–60 cycles when cycled at 0.12 C in the voltage range 0.005–0.8 V vs. Li.

Experimental

Commercial SnO (Acros Organics, 98%), V_2O_3 (Acros Organics, 99%), and VO (Alfa Aesar, 99%) were employed to prepare the nano-composites. Appropriate amounts (~2.5 g in each case) were weighed and transferred to stainless steel vial inside in an Ar-filled glove box (MBraun, Germany), sealed and taken out for HEB at 1,400 rpm using the equipment Spex, 8000D, USA. Stainless steel balls were used for milling with a ball-to-active mass ratio of 4:1. Ball milling was carried out for 18 h, in three steps of 6 h each, to avoid significant rise in temperature of the vial. After milling, the vials containing the nano-composites were opened in the glove box,

collected, and kept in a desiccator. For the sake of convenience, the nano-composites prepared by HEB are referred as nano-SnO, nano-SnO($V_2O_3)_x$ (x=0.25, 0.50), and nano-SnO(VO)$_{0.5}$.

Structural and morphological characterizations were carried out by X-ray diffractometer (Philips, Expert) equipped with CuKα radiation, field emission scanning electron microscope (SEM; JEOL JSM-6700F), and high-resolution transmission electron microscope (HR-TEM; JEOL JEM 3010 operating at 300 kV). Chemical analysis for Fe and Cr of selected nano-composites was performed by inductively coupled plasma optical emission spectrometer (ICP-OES) system (Perkin Elmer Dual-View Optima 5300 DV). The composites were dissolved in an acid mixture using Milestone Microwave Laboratory System for the analysis. The electrodes for electrochemical studies were fabricated by mixing the active material, super P carbon powder (electronically conducting additive), and polymer binder (Kynar 2801) in the weight ratio, 70:15:15. N-Methyl-pyrrolidinone was used as the solvent for the binder. The homogeneous and viscous slurry obtained after thorough mixing by a magnetic stirrer was coated onto an etched Cu foil (15 μm thick, Alpha Industries Co. Ltd., Japan) to form a thick layer (~15 μm) by doctor-blade technique. The coated Cu substrate was then dried at 70 °C to evaporate the solvent, pressed between stainless steel rollers, and was then cut into disks. The active mass in the electrode is typically 3 to 4 mg, and the geometrical area of the electrode is 2.0 cm^2. The electrode disks were vacuum-dried at 70 °C for 12 h and cooled before being transferred into an Ar-filled glove box for cell assembly. The atmosphere in the glove box was maintained at <1 ppm of H$_2$O and O$_2$. For the coin-cell (size 2016) assembly, a glass microfiber filter (GF/F) (Whatman Int. Ltd, Maidstone, England) was used as the separator, and the electrolyte used was 1 M LiPF$_6$ dissolved in ethylene carbonate + dimethyl carbonate (DMC) in the ratio of 1:1 volume (Merck). The Li metal foil (Kyokuto Metal Co., Japan) was cut into circular disk (16 mm diameter) and used as the counter/reference electrode. More details on the cell fabrication can be found in our previous work [26, 27].

Cyclic voltammetry and galvanostatic cycling tests were conducted at room temperature (24 °C) using a potentiostat system (Mac-pile II, Bio-logic, France) and Bitrode multiple battery tester (Model SCN, Bitrode, USA), respectively. The cells were aged for 12 h before testing to ensure percolation of the electrolyte into the composite electrode. For ex situ X-ray diffraction (XRD), three identical cells were fabricated: one was discharged to 0.5 V, another one to 0.05 V, and the third cell was charged to 0.8 V after complete discharge at 0.12 C, during the first cycle and equilibrated for 3 to 4 h. The cells were transferred to Ar-filled glove box and

dismantled. The recovered electrodes were washed with DMC, dried, and covered by Para-film "M" (American National Can™, USA) to avoid contact with air and taken out of the glove box for mounting on the XRD equipment.

Results and discussion

Structure and morphology

The powder XRD pattern of SnO-C (commercial) is shown in Fig. 1a. It is indexed as per the tetragonal structure (space group, P4/nmm). The lattice parameters, calculated by the Rietveld refinement (Topas R 2.1 software), are a=3.801 (2)Å and c=4.835 (2)Å. These agree with those reported in the JCPDS card no 85-0712. Figure 1b shows the XRD pattern of nano-SnO. Surprisingly, the XRD pattern shows the characteristic lines of SnO$_2$ (JCPDS card no. 77-0452) and Sn metal (JCPDS card no. 04-0673), and the lines due to SnO are completely absent. This can be ascribed to the disproportionation of SnO by self-oxidation–reduction during the HEB in Ar atmosphere as per Eq. 1.

$$2\,SnO \rightarrow SnO_2 + Sn \tag{1}$$

The forward reaction of Eq. 1 is energetically favorable due to negative Gibbs free energy change ($\Delta G^0_{298} = -5.9$ kJmol^{-1}) and is aided by moderately mild temperatures [28]. It is well known that HEB gives rise to local heating of the material particles, to temperatures as high as 500–600 °C, and this can enhance the rate of reaction of
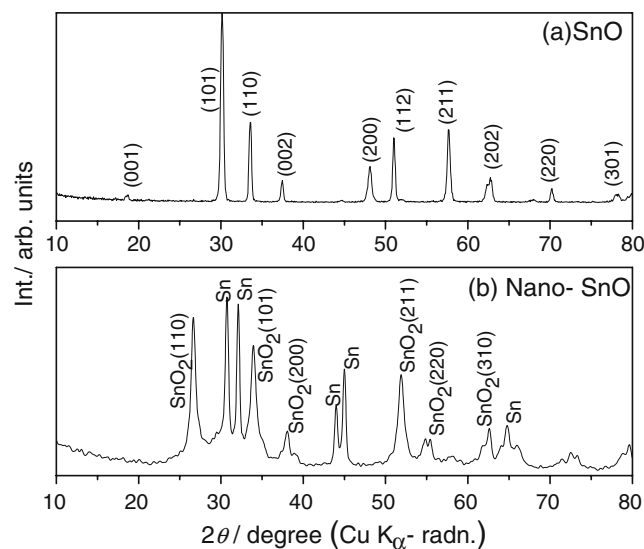

Fig. 1 Powder X-ray diffraction patterns. **a** SnO (commercial) and **b** nano-SnO (after high-energy ball milling). Miller indices (*h k l*) are shown

Eq. 1. Thus, it is concluded that SnO is unstable to HEB in an inert atmosphere.

Figure 2a shows the XRD pattern of nano-SnO $(V_2O_3)_{0.25}$. It shows only lines due to tetragonal SnO_2 (JCPDS card no. 77-0452) except for a very small amount of SnO (peak at $2\theta=30.2°$). The nano-SnO$(V_2O_3)_{0.5}$ also showed a similar XRD pattern (figure not shown). As SnO is a good reducing agent, it forms SnO_2 by reducing V_2O_3 to its lower valency state (VO_x, $x\sim1.0$). No lines due to Sn metal are seen. Thus, the composite consists of $SnO_2.VO_x$. Figure 2b shows the XRD pattern of nano-SnO$(VO)_{0.5}$, and as can be seen, lines due to both SnO_2 and Sn metal are present, as can be expected because VO cannot be reduced to V metal by SnO. Thus, the composite consists of $SnO_2.Sn.VO_x$ ($x\sim1$), and Figs. 1b and 2b bear good resemblance. In the XRD patterns of nano-SnO$(V_2O_3)_{0.25}$ and nano-SnO$(VO)_{0.5}$, lines due to VO_x are not seen, possibly due to their amorphous nature, as a result of HEB. It may be pointed out that Park et al. [22] did not notice lines due to TiO_2 in their composite Sn.TiO_2.C prepared by the ball milling of SnO.Ti.C. It is known that HEB of reactants employing stainless balls and vials gives rise to Fe and Cr metal impurities as a result of non-negligible deterioration of the components. Lee et al. [29] during their studies on the synthesis of Ti–Si and Ti–Si–Al alloys by HEB noticed ~5 and ~1 at.% of Fe and Cr, respectively, as impurities after 20 h of HEB. In the present study, chemical analysis of nano-SnO$(V_2O_3)_x$ ($x=$ 0.25 and 0.5) and SnO$(VO)_{0.5}$ by ICP-OES yielded ~0.9–

3.3 and ~0.1–0.2 wt.% of Fe and Cr, respectively, depending on the value of x. The XRD patterns did not reveal any lines due to the Fe and Cr metals in the above composites, due to their small content and amorphous nature.

Figure 3a shows the SEM photograph of nano-SnO $(VO)_{0.5}$ with a flake-type morphology containing agglomerated particles. The TEM photograph of nano-SnO$(V_2O_3)_{0.25}$, shown in Fig. 3b, also indicates the agglomeration of nano-particles of size 20–30 nm. The crystallite sizes of nano-SnO and nano-SnO$(V_2O_3)_{0.25}$ were calculated by using the Scherrer's formula, $P = K\lambda/(\beta_{1/2}\cos\theta)$, where P is crystallite size, K is Scherrer constant (0.9), λ is the wavelength of CuKα radiation (1.54059Å), $\beta_{1/2}$ is the full width at half maximum (FWHM) in radians of the XRD peak, and θ is the scattering (Bragg) angle [12]. The XRD instrumental broadening was calculated by using the nano-TiO_2 (anatase; Evonik Degussa; 99.5%) of ~25 nm particle size as the standard and was found to be 0.08°. For TiO_2, we assume the crystallite size is of the same order as particle size. The crystallite sizes of the composites were calculated by using $\beta_{1/2}$ (FWHM) values of two or three high-intensity peaks and the corresponding θ values in the XRD patterns (Figs. 1b and 2a). The average crystallite sizes (P) obtained are nano-SnO 12 (±3 nm) and nano-SnO $(V_2O_3)_{0.25}$ 13 (±3 nm), thereby confirming the nano-nature of the composites prepared by HEB.

Electrochemical studies

Galvanostatic cycling of nano-SnO

The capacity–voltage profiles of discharge and charge cycles of nano-SnO at a current density 60 mAg^{-1} (0.12 C) in the voltage range of 0.005–0.8 V vs. Li up to 50 cycles are shown in Fig. 4a, b. Only selected cycles are shown for clarity. The first-discharge profile (Fig. 4a) commenced from the open circuit voltage (OCV ~2.0 V) to the lower cutoff voltage 0.005 V. The voltage drops continuously and a broad plateau at ~0.9 V followed by a continuous sloping region is noticed up to the voltage of 0.005 V. This is expected since the nano-SnO consists of the composite Sn.SnO_2. Amorphization/crystal structure destruction of SnO_2 will occur according to Eq. 2. At the same time, alloying reaction of Sn will also occur as per Eq. 3, thus giving rise to a small voltage plateau at ~0.4 V and a continuously sloping profile is noticed till the end of discharge. The total first-discharge capacity is 1,500(±5)mAhg^{-1} (7.5 mol of Li per mole of nano-SnO). The expected first-discharge capacity according to Eqs. 2 and 3 is only 6.4 mol of Li. The extra consumption of 1.1 mol of Li can be ascribed to the solid-electrolyte interphase formation [9, 12, 14, 15, 30].
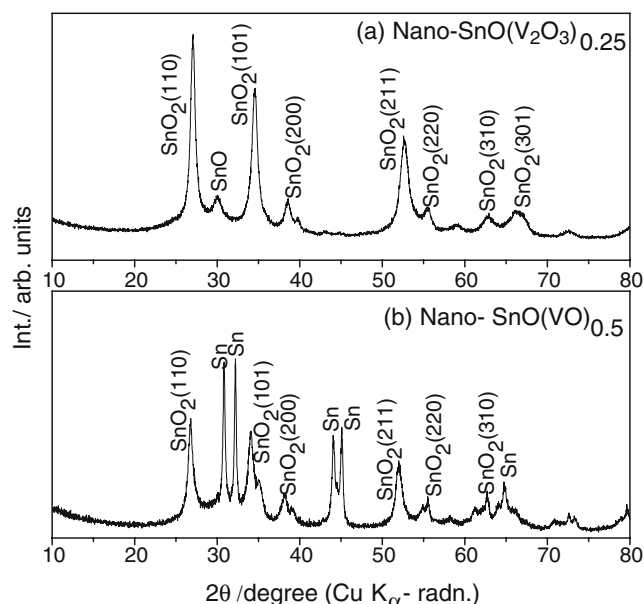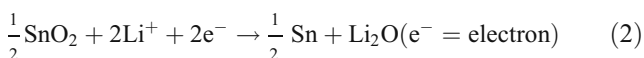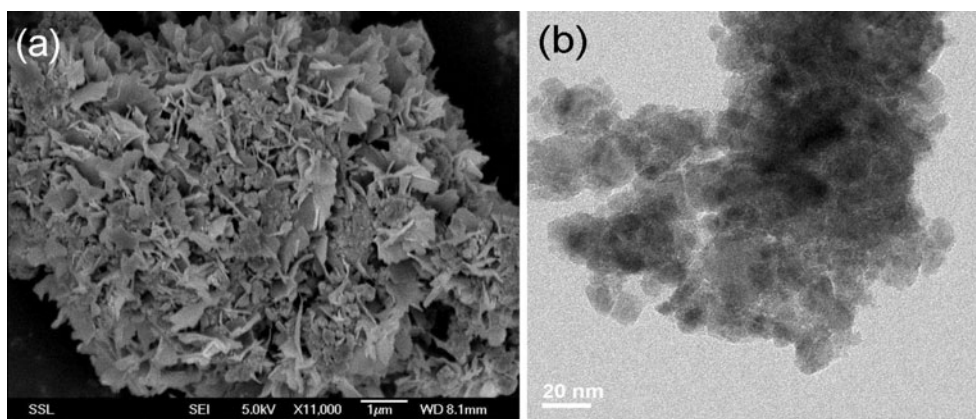
Fig. 2 Powder X-ray diffraction patterns. **a** Nano-SnO$(V_2O_3)_{0.25}$ and **b** nano-SnO$(VO)_{0.5}$. Miller indices ($h\,k\,l$) are shown

$$\frac{1}{2}SnO_2 + 2Li^+ + 2e^- \rightarrow \frac{1}{2}Sn + Li_2O(e^- = electron) \qquad (2)$$

$$Sn + 4.4Li \rightleftharpoons Li_{4.4}Sn \qquad (3)$$

During the first charge, a broad voltage plateau is noticed at ~0.6 V corresponding to the de-alloying reaction (Eq. 3; Fig. 4a). The total first-charge capacity is $575(\pm5)$ mAhg^{-1} (2.9 mol of Li), with a net ICL value $925(\pm5)$mAh g^{-1} (4.6 mol of Li). The discharge–charge profiles between two and 50 cycles are analogous to that of the first-charge profile. It is clear from Figs. 4b and 5a (capacity vs. cycle number plot) and the data presented in Table 1 that large capacity fading occurs in nano-SnO and between 10 and 50 cycles and the total loss is 59%. These results are in agreement with those reported on micro-SnO and nano-SnO in the literature [9, 15, 17].

Galvanostatic cycling of composites nano-SnO(VO$_x$)

The capacity–voltage profiles of nano-SnO$(V_2O_3)_{0.25}$ at 60 mAg^{-1} (0.12 C) in the voltage range 0.005–0.8 V are shown in Fig. 6a, b. As discussed earlier, the nano-composite consists of SnO$_2$.VO$_x$. The first discharge starts from the OCV (~2.5 V), and broad voltage plateaus at ~1.0 and ~0.7 V are noticed until a capacity of $900(\pm5)$mAhg^{-1} (consumption of 5.8 mol of Li per mole of composite) is reached. This is followed by a minor plateau at ~0.2 V, at the end of which a total capacity of $1,915(\pm5)$mAhg^{-1} (12.3 mol of Li) is obtained (Fig. 6a; Table 1). The voltage plateaus at ~1.0 and ~0.7 V may correspond to the structure destruction of SnO$_2$ and formation of Sn metal, and the plateau at ~0.2 V corresponds to the alloy formation Li$_{4.4}$Sn (Eq. 3). The theoretical first-discharge capacity, as per Eqs. 3 and 4, is 1,075 mAhg^{-1} (6.9 mol of Li; Fig. 6a; Table 1).

$$SnO(V_2O_3)_{0.25} + 2.5Li^+ + 2.5e^- \rightarrow Sn + 0.5VO + 1.25Li_2O$$
$$(4)$$
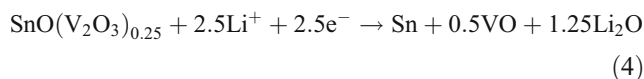
During the first-charge cycle, a broad voltage plateau, which is due to the de-alloying reaction of Li$_{4.4}$Sn, onsets at ~0.6 V (Fig. 6a). The total first-charge capacity is $500(\pm5)$mAhg^{-1} (3.2 mol of Li per mole of composite), whereas 685 mAhg^{-1} (4.4 mol of Li) is expected theoretically. The second-discharge profile is different from the first-discharge profile, where only a sloping region is noticed from ~0.7 to ~0.2 V and another sloping

Fig. 4 Galvanostatic discharge–charge profiles of nano-SnO: a first cycle and b two to 50 cycles. The *numbers* indicate cycle number. Voltage range 0.005–0.8 V vs. Li at a current density of 60 mAg^{-1} (0.12 C)
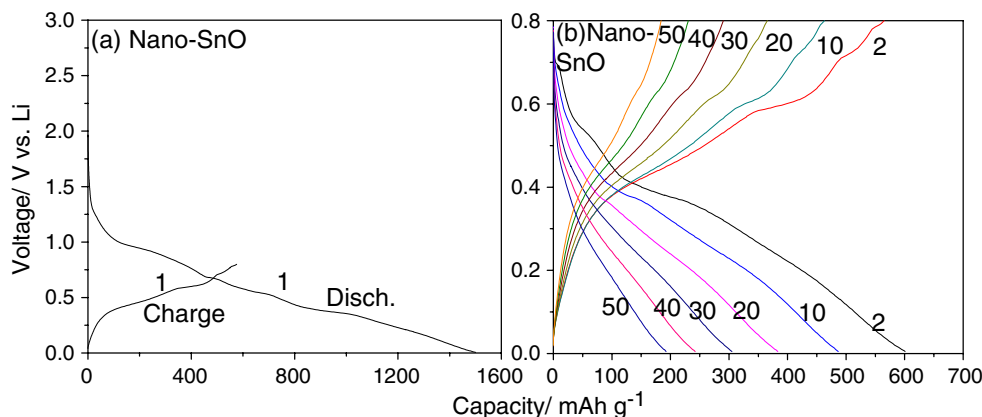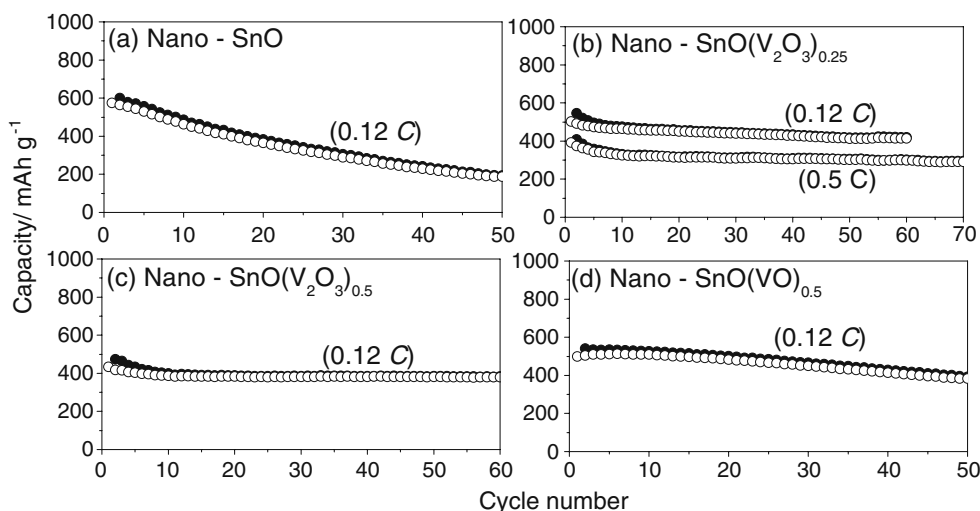
Fig. 5 Capacity vs. cycle number plots. **a** Nano-SnO, **b** nano-SnO(V_2O_3)$_{0.25}$ at 0.12 and 0.5 C (1 C=500 mA g^{-1}), **c** nano-SnO(V_2O_3)$_{0.5}$, and **d** nano-SnO(VO)$_{0.5}$. Voltage range 0.005–0.8 V vs. Li, at current density of 60 mA g^{-1} (0.12 C). *Filled symbols* discharge capacity, *open symbols* charge capacity

region till 0.005 V (Fig. 6b). The total second-discharge capacity is 545($\pm$5) mAh g^{-1} (3.5 mol of Li). The charge profiles in the range two to 60 cycles are analogous to the first-charge profile establishing the same reaction mechanism, i.e., de-alloying of Li$_{4.4}$Sn formed during the discharge reaction. The capacity vs. cycle number plot, shown in Fig. 5b, indicates small capacity fading between 10 and 50 cycles corresponding to the loss of 11%, and the coulombic efficiency reaches 96–98% (Table 1). The capacity contribution due to the VO$_x$ present in the nano-composite can be neglected because our unpublished results show that ball-milled V$_2$O$_3$ shows only 75($\pm$5) mAh g^{-1} at 60 mA g^{-1} when cycled in the voltage range 0.005–0.8 V and this includes the conducting carbon contribution.

Galvanostatic cycling was also carried out with an upper cutoff voltage of 1.0 V at 60 mA g^{-1}. The voltage–capacity profiles (figure not shown) are analogous to the profiles in the range of 0.005–0.8 V. The observed first-discharge capacity is 1,810($\pm$5) mAh g^{-1} (11.6 mol of Li), whereas the first-charge capacity is 565($\pm$5) mAh g^{-1} (3.6 mol of Li) with the observed ICL being 1,245($\pm$5) mAh g^{-1} (8 mol of Li). The reversible capacity at the end of 40th cycle is 450 ($\pm$5) mAh g^{-1} (2.9 mol of Li; Table 1). Capacity fading occurs similar to the cycling behavior with the upper cutoff voltage of 0.8 V, and the capacity fade is 14% between five and 40 cycles (Table 1). The rate capability of nano-SnO (V$_2$O$_3$)$_{0.25}$ was tested on a duplicate cell at a current rate of 0.5 C (250 mA g^{-1}) in the voltage range of 0.005–0.8 V up to 70 cycles (Fig. 5b). The initial capacities during first-discharge and first-charge cycle are 1,760($\pm$5) mAh g^{-1} (11.3 mol of Li) and 390($\pm$5) mAh g^{-1} (2.5 mol of Li), respectively. A capacity of 330–300($\pm$5) mAh g^{-1} (1.9 mol of Li) is observed in the range 10–70 cycles with a capacity fade of only 10% (Table 1; Fig. 5b).

The capacity–voltage profiles of nano-SnO(V$_2$O$_3$)$_{0.5}$ at 60 mA g^{-1} (0.12 C) in the voltage range 0.005–0.8 V are similar to those observed for nano-SnO(V$_2$O$_3$)$_{0.25}$ (figure not shown). The first-discharge capacity is 1,850($\pm$5) mAh g^{-1} (14.5 mol of Li), and the first-charge capacity is 435 ($\pm$5) mAh g^{-1} (3.4 mol of Li). The observed ICL (1,415 mAh g^{-1}; 11.2 mol of Li) is larger in comparison to that found in nano-SnO(V$_2$O$_3$)$_{0.25}$, as can be expected due to the increased content of V-oxide. The reversible capacity showed a slight decrease up to 10 cycles and stabilized to 380($\pm$5) mAh g^{-1} (3 mol of Li) up to 60 cycles, with no noticeable capacity fading (Fig. 5c; Table 1).

Figure 6c, d shows the capacity–voltage profiles of nano-SnO(VO)$_{0.5}$ at 60 mA g^{-1} (0.12 C) in the voltage range 0.005–0.8 V up to 50 cycles. The profiles are analogous to those measured on nano-SnO and contain Sn, SnO$_2$, and VO$_x$ as a result of ball milling. The total first-discharge capacity is 1,375($\pm$5) mAh g^{-1} (8.6 mol of Li) which is larger than the expected value 1,020 mAh g^{-1} (6.4 mol of Li). During the first charge, a broad voltage plateau at ~0.45 V followed by two more small plateau regions at ~0.6 and ~0.7 V is seen. These plateaus are due to the de-alloying reaction to form Sn metal particles. These plateau regions persist in subsequent cycles (up to 20) as is clear in Fig. 6d and are almost similar to the profiles shown by nano-SnO (Fig. 4b). The total first-charge capacity is 500($\pm$5) mAh g^{-1} (3.1 mol of Li). Thus, the ICL during the first cycle is 875($\pm$5) mAh g^{-1} (5.5 mol of Li). The second-discharge and second-charge profiles are analogous to the first-discharge and first-charge profiles and show total capacities of 540($\pm$5) mAh g^{-1} (3.4 mol of Li) and 505($\pm$5) mAh g^{-1} (3.2 mol of Li), respectively. The reversible capacity remains stable up to 10 cycles but decreases thereafter. At the end of 50th

Table 1 Theoretical and observed capacities (corresponding number of moles of Li per formula unit) of nano-SnO and nano-SnO(VO$_x$) composites

Composite (formula weight)	Theoretical capacity, mAh g⁻¹ (moles of Li)		Observed capacity, (±5) mAh g⁻¹				Capacity fading (%; 10–50cycles)
	1st discharge	Reversible capacity (4.4 Li)	1st discharge	1st charge	50th discharge	50th charge	
Nano-SnO (134.7 g)	1,275 (6.4 Li)	875	1,500 (7.5 Li)	575 (2.9 Li)	195 (0.98 Li)	190 (0.95 Li)	59
Nano-SnO(V$_2$O$_3$)$_{0.25}$ (172.2g)	1,075 (6.9 Li)	685	1,915 (12.3 Li)	500 (3.2 Li)	415 (2.7 Li)	410 (2.6 Li)	11
Nano-SnO(V$_2$O$_3$)$_{0.25}$ current rate 0.5 C	1,075 (6.9 Li)	685	1,760 (11.3 Li)	390 (2.5 Li)	295 (1.9 Li; 70th cycle)	290 (1.86 Li; 70th cycle)	10 (10–70 cycles)
Nano-SnO(V$_2$O$_3$)$_{0.25}$ voltage range 0.005–1.0 V	1,075 (6.9 Li)	685	1,810 (11.6 Li)	565 (3.6 Li)	450 (2.9 Li; 40th cycle)	445 (2.8 Li; 40th cycle)	14 (5–40 cycles)
Nano-SnO(V$_2$O$_3$)$_{0.5}$ (209.6 g)	940 (7.4)	562	1,850 (14.5 Li)	435 (3.4 Li)	385 (3.1 Li)	380 (3.0 Li)	Nil
Nano-SnO(VO)$_{0.5}$ (168.2 g)	1,020 (6.4 Li)	700	1,375 (8.6 Li)	500 (3.1 Li)	390 (2.45 Li)	380 (2.4 Li)	25
Nano-SnO(VO)$_{0.5}$ voltage range 0.005–1.0 V	1,020 (6.4 Li)	700	1,600 (10 Li)	630 (4 Li)	480 (3 Li; 40th cycle)	460 (2.9 Li; 40th cycle)	28 (5–40 cycles)

Voltage range 0.005–0.8 V vs. Li at a current density 60 mA g⁻¹ (0.12 C; 1 C=500 mA g⁻¹)

cycle, the capacity is 380(±5)mAhg⁻¹ (2.4 mol of Li) which corresponds to a capacity fade of 25% between five and 50 cycles (Fig. 5d; Table 1). The capacity–voltage profiles of nano-SnO(VO)$_{0.5}$ in the voltage range 0.005–1.0 V at 60 mAg⁻¹ (figure not shown) are similar to the profiles in the voltage range 0.005–0.8 V. The total first-discharge capacity is 1,600(±5)mAhg⁻¹ (10 mol of Li), whereas the first-charge capacity is 630(±5)mAhg⁻¹ (4 mol of Li). The reversible capacity at the end of 40th cycle is 460(±5)mAhg⁻¹ (2.9 mol of Li), showing a capacity fade of 28% between five and 40 cycles (Table 1). Thus, cycling of nano-SnO(VO)$_{0.5}$ to an upper cutoff voltage of 1.0 V gave only a small increase in capacity, but the capacity-fading behavior is similar to that encountered when cycled to 0.8 V cutoff.

From Fig. 5 and Table 1, the following conclusions can be drawn: (1) Nano-SnO shows capacity fading on cycling up to 50 cycles at 0.12 C rate in the voltage range 0.005–0.8 V vs. Li. It shows a large capacity fading (59% between 10 and 50 cycles), possibly due to the presence of nano-Sn metal and nano-SnO$_2$ as a result of HEB of SnO. Hence, nano-SnO or (Sn.SnO$_2$), without any matrix element, shows capacity fading, and this result is in agreement with several reports on the Li cycling of micro- and nano-SnO in the literature [9, 14–17, 19]. (2) Nano-SnO(V$_2$O$_3$)$_{0.25}$ shows smaller reversible capacity in comparison to nano-SnO, as can be expected due to the presence of matrix of VO$_x$. This nano-composite consisting of SnO$_2$.VO$_x$ shows capacity fading under the above cycling conditions, with a loss of only 11% between 10 and 50 cycles. The nano-composite with a higher content of V$_2$O$_3$, namely nano-SnO(V$_2$O$_3$)$_{0.5}$, shows no noticeable capacity fading up to at least 60 cycles. Thus, increasing the VO$_x$ content with respect to Sn content has a profound effect on the Li cyclability of the nano-composite. (3) The nano-composite with VO as the matrix, namely nano-SnO(VO)$_{0.5}$, shows capacity fading of 25%, in comparison to the value of 11% encountered in nano-SnO(V$_2$O$_3$)$_{0.25}$, even though the nominal VO$_x$ content in both the composites is the same. This is understandable because the latter phase is composed of (SnO$_2$.VO$_x$) whereas the former phase is composed of (Sn.SnO$_2$.VO$_x$). Here, we may mention that the effect of Fe/Cr impurities, noticed as a result of HEB, on the electrochemical behavior of the nano-composites is negligible since they do not form alloys with Li metal. Further, because the upper cutoff voltage for cycling is 0.8 V, no oxidation of Fe/Cr can occur at this voltage by the "conversion reaction" (Fe + Li$_2$O ⇌ FeO + 2 Li). Thus, it is concluded that both nano-size SnO$_2$ and inactive matrix (VO$_x$) mutually help each other to buffer the large unit cell volume variations and help in better Li cycling via Eq. 3, and the Sn–V ratio of 1:1, as in nano-SnO(V$_2$O$_3$)$_{0.5}$, is found to be the optimum.

Fig. 6 Galvanostatic discharge–charge profiles. Nano-SnO(V$_2$O$_3$)$_{0.25}$: **a** first cycle and **b** two to 50 cycles. Nano-SnO(VO)$_{0.5}$: **c** first cycle and **d** two to 50 cycles. The *numbers* indicate cycle number. Voltage range 0.005–0.8 V vs. Li at a current density of 60 mA g^{-1} (0.12 C)
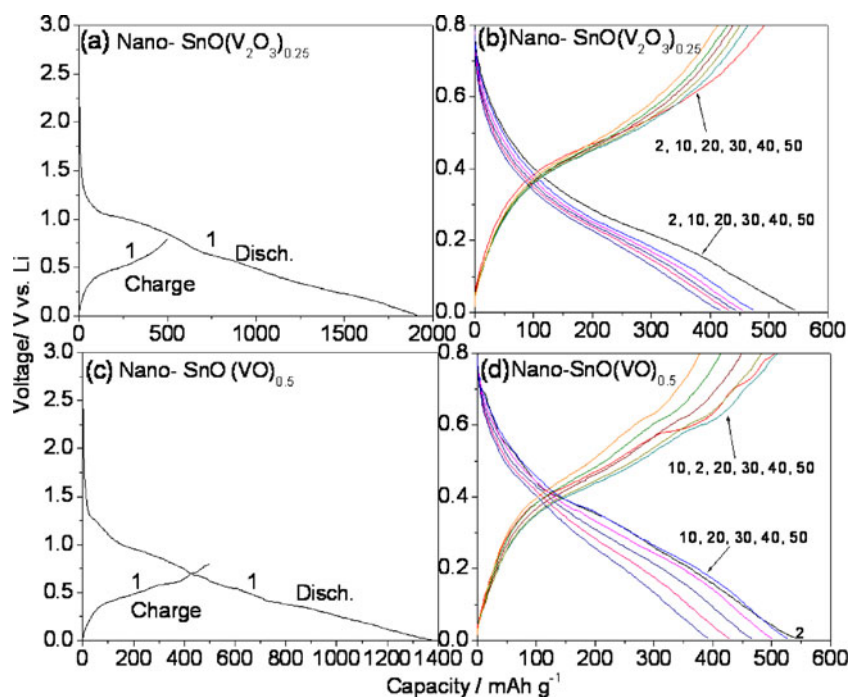
Cyclic voltammetry

Cyclic voltammetry, a complementary tool to galvanostatic cycling performance, is commonly employed to establish the reversibility of electrode materials vs. Li and to evaluate the potentials at which the discharge–charge reactions take place. Cyclic voltammograms (CV) of nano-SnO(V$_2$O$_3$)$_{0.5}$ and nano-SnO(VO)$_{0.5}$ at the slow scan rate of 58 μVs^{-1} in the potential range of 0.005–0.8 V were recorded up to 40 cycles and up to 6 cycles, respectively, and are shown in Fig. 7. The Li metal acts as the counter and reference electrode.

The first cathodic scan of nano-SnO(V$_2$O$_3$)$_{0.5}$ started from an OCV (~3.0 V), with a broad peak at ~0.8 V, which corresponds to the crystal structure destruction and formation of Sn nano-particles embedded in VO and Li$_2$O amorphous matrix (Eq. 4; Fig. 7a). This is followed by a shoulder peak at 0.4 V and a broad peak centered at 0.14 V. These two peaks correspond to the alloying of Sn in stages to reach the composition Li$_{4.4}$Sn (forward reaction of Eq. 3). During the first anodic scan, a broad peak at 0.56 V is seen, which corresponds to de-alloying reaction to form Sn metal nano-particles. The second cathodic scan is similar to the first cathodic scan except for the absence of the shoulder peak at ~0.4 V. Between two and 40 cycles, the anodic peak shifted to a slightly lower potential value (~0.5 V), which indicates that the de-alloying reaction occurs at lower potential due to nano-size effect and "conditioning" of the electrode. The average charge and discharge potentials noticed from CV are ~0.5 and ~0.2 V,
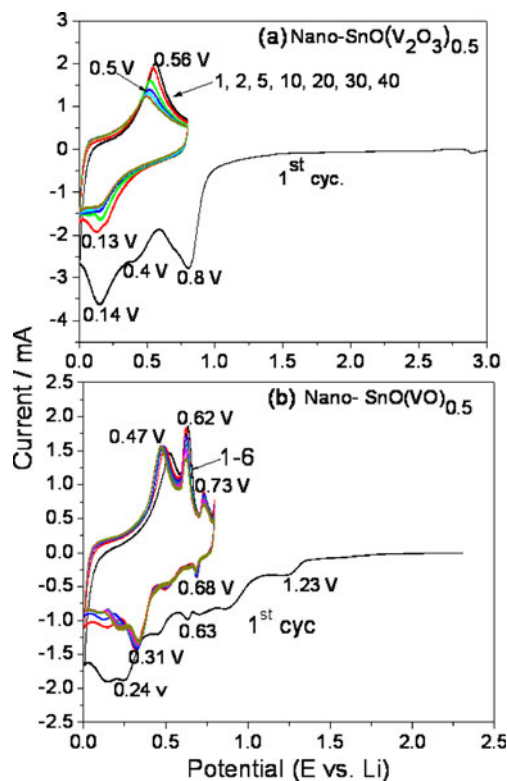

Fig. 7 Cyclic voltammograms of **a** nano-SnO(V$_2$O$_3$)$_{0.5}$, one to 40 cycles, and **b** nano-SnO(VO)$_{0.5}$, one to six cycles. Scan rate 58 μVs^{-1}. Li metal anode was the counter and reference electrode. *Numbers* represent the potentials in volts. *Integer numbers* represent cycle numbers

respectively, which match well with the voltage plateaus seen in the galvanostatic charge–discharge profiles. The areas under the peaks in the CVs decrease slowly from two to 10 cycles showing slow capacity fading. On the other hand, the areas under the peaks from 11 to 40 cycles are almost the same which indicate almost nil capacity fading and this is corroborated by the galvanostatic data (Fig. 5c).

The CVs of nano-$SnO(VO)_{0.5}$ are shown in Fig. 7b. The first cathodic scan started from the OCV (~2.3 V) and showed several low-intensity peaks in the potential range 0.4–1.2 V. The crystal structure destruction (amorphization of lattice) to form Sn nano-particles embedded in VO and Li_2O occurs in this potential region and, as mentioned earlier, XRD shows that the nano-composite consists of Sn. SnO_2.VO. The first cathodic scan also shows a broad split peak centered at 0.24 V, which corresponds to the alloy ($Li_{4.4}Sn$) formation. The first anodic scan shows medium-intensity peaks at 0.47 and 0.62 V and a low-intensity peak at 0.73 V. These peaks correspond to the de-alloying reaction to form Sn metal nano-particles and seem to occur in stages. The second cathodic scan differs from the first cathodic scan in that the low-intensity peaks are seen at 0.68 and ~0.5 V and the split peak is now centered at 0.31 V. This shows that alloying reaction is occurring in stages. The CVs of two to six cycles not only overlap well showing good reversibility but also indicate capacity fading due to the decrease in the areas under the peaks from two to six cycles. The CV peaks are reflected as voltage plateaus in the galvanostatic profiles in Fig. 6c, d. The CVs of nano-SnO (figure not shown) are analogous to those observed in nano-$SnO(VO)_{0.5}$, thereby indicating that VO_x is not participating in the Li-cycling behavior in the composites and acts only as an electrochemically inactive but electronically conducting matrix.

A comparison of CVs of Fig. 7a, b clearly reveals the difference in cycling behavior of electrochemically formed nano-particles of Sn (via Eq. 2) and that of nano-Sn obtained by the HEB process. Figure 7a shows only one well-defined cathodic and anodic peak indicating that the alloying–de-alloying reaction (Eq. 3) takes place in a continuous fashion. The fine structure, by way of additional cathodic and anodic peaks noticed in Fig. 7b for the nano-$SnO(VO)_{0.5}$, is due to the alloying–de-alloying reaction of nano-Sn (along with SnO_2) formed during the ball-milling process. Studies by Courtney et al. [31] on the Li–Sn system and by Park and Sohn [32] and Hassoun et al. [33] on the nano-composite Sn-C have shown that, whenever Sn metal is used as the active material, the alloying–de-alloying reaction always goes through several stages, depending on the value of y from 0 to 4.4 in Li_ySn at various fixed potentials ranging from 0.2 to 0.8 V vs. Li. Indeed, the observed anodic peaks at 0.62 and 0.73 V in Fig. 7b correspond to y=1.75–2.5 and 1.0,

respectively [31]. The matrix (VO_x, $x \sim 1$) is not able to buffer the volume changes occurring, in stages, during the reactions of Eq. 3 in nano-$SnO(VO)_{0.5}$ and hence the observed capacity fading on cycling (Fig. 5d). On the other hand, VO_x is able to buffer the volume changes occurring during cycling of nano-$SnO(V_2O_3)_{0.5}$ since no stages were observed in the alloying–de-alloying reactions of Eq. 3 (Fig. 5c). To summarize, the CV studies corroborate the galvanostatic cycling data and clearly distinguish between the cycling behavior of electrochemically generated Sn and that produced in the nano-composite as a result of HEB.

Ex situ XRD of nano-$SnO(V_2O_3)_{0.25}$

To establish the reaction mechanism and to supplement the galvanostatic and CV data, ex situ XRD studies were performed on the multiple cells of nano-$SnO(V_2O_3)_{0.25}$ at selected discharge/charge voltages during the first cycle. The ex situ XRD patterns are shown in Fig. 8. The y-axis values have been normalized for better comparison. The pattern of bare electrode (Fig. 8 a) shows the characteristic lines of SnO_2, similar to that of Fig. 2a, along with the Cu metal lines due to the substrate. The pattern at 0.5 V during the first discharge shows the characteristic lines of Sn metal due to the reaction of SnO_2/SnO with Li metal as per Eq. 4 (Fig. 8 b). This is in accord with galvanostatic and CV data. The pattern at 0.05 V (Fig. 8 c) shows the characteristic lines of both Li–Sn alloy ($2\theta=20–25^0$) and Sn metal ($2\theta=30–35^0$) as per the forward reaction of Eq. 3, which is expected to be completed upon deep discharge to 0.005 V. The XRD pattern at 0.8 V at the end of first charge, shown in Fig. 8 d, does not show the lines of Sn metal (reverse reaction of Eq. 3), possibly due to the nano-size nature of
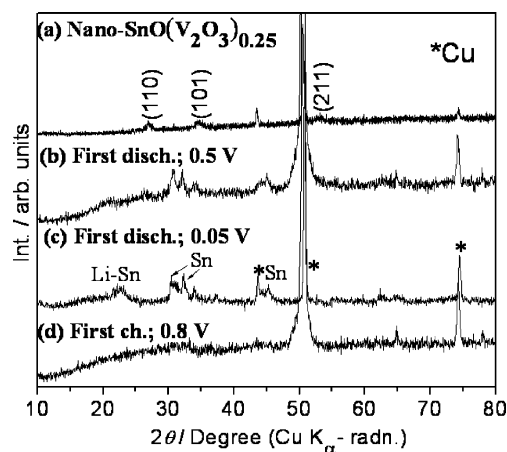

Fig. 8 Ex situ XRD patterns of nano-$SnO(V_2O_3)_{0.25}$. *a* Bare electrode, *b* during first discharge at 0.5 V, *c* during first discharge at 0.05 V, and *d* during first charge at 0.8 V vs. Li

the particles. Thus, the ex situ XRD measurements corroborate the galvanostatic and CV data and lend support to the Li-cycling mechanism.

Conclusions

The nano-composites $SnO(V_2O_3)_x$ ($x=0$, 0.25, and 0.5) and $SnO(VO)_{0.5}$ are prepared from SnO and V_2O_3/VO by HEB and are characterized by XRD, SEM, and HR-TEM techniques. Interestingly, SnO and $SnO(VO)_{0.5}$ are not stable to HEB and undergo self-oxidation–reduction to give Sn and SnO_2. Ball milling of $SnO(V_2O_3)_x$ gives rise to a nano-composite of SnO_2 and VO_x. The Li-cycling properties are evaluated by galvanostatic discharge–charge cycling and cyclic voltammetry with Li as the counter electrode at room temperature. The nano-$SnO(V_2O_3)_{0.5}$ showed a first-charge capacity of $435(\pm5)$ mAh g^{-1} which stabilized to $380(\pm5)$ mAh g^{-1} with no noticeable fading in the range of 10–60 cycles when cycled at 60 mA g^{-1} (0.12 C) in the voltage range 0.005–0.8 V. Under similar cycling conditions, nano-SnO, nano-$SnO(V_2O_3)_{0.25}$, and nano-$SnO(VO)_{0.5}$ showed initial reversible capacities between 630 and $390(\pm5)$ mAh g^{-1}. Between 10 and 50 cycles, nano-SnO showed a capacity fade as high as 59% in good agreement with literature reports, whereas the above two VO_x-containing composites showed capacity fade ranging from 10% to 28%. Cycling to an upper cutoff voltage 1.0 V gives rise to a slight increase in the reversible capacity in the case of nano-$SnO(V_2O_3)_{0.25}$ and nano-$SnO(VO)_{0.5}$. However, capacity fading also increased in them in comparison to the performance with 0.8 V cutoff (Table 1). The coulombic efficiency increased in all the nano-composites to 96–98% after 10 cycles. The presence of matrix (VO_x) enhances the Li-cycling behavior by buffering the unit cell volume variations and providing an electronically conducting network to Li diffusion in the nano-composites. The observed galvanostatic cycling, CV, and ex situ XRD data have been interpreted in terms of the alloying–de-alloying reaction of Sn in the nano-composite "Sn-VO_x-Li$_2$O". In all the nano-composites presently studied, the average discharge (alloying) potential is 0.2–0.3 V and average charge (de-alloying) potential is 0.5–0.6 V vs. Li, in good agreement with literature. It is concluded that, upon further optimization, the nano-$SnO(VO_x)$ can be a prospective anode material for future generation LIBs.

References

1. Nazri G-A, Pistoia G (eds) (2003) Lithium batteries: science and technology. Kluwer Academic, New York
2. Arico AS, Bruce P, Scrosati B, Tarascon J-M, Schalkwijk WV (2005) Nat Mater 4:366
3. Shukla AK, Kumar TP (2008) Curr Sci (India) 94:314
4. Ma H, Cheng F, Chen J, Zhao J, Li C, Tao Z, Liang J (2007) Adv Mater 19:4067
5. Bruce PG, Scrosati B, Tarascon J-M (2008) Angew Chem Int Ed 47:2930
6. Kim MG, Cho J (2009) J Electrochem Soc 156:A277
7. Kim H, Han B, Choo J, Cho J (2008) Angew Chem Int Ed 47:10151
8. Larcher D, Beattie S, Morcrette M, Edström K, Jumas J-C, Tarascon J-M (2007) J Mater Chem 17:3759
9. Aurbach D, Nimberger A, Markovsky B, Levi E, Sominski E, Gedanken A (2002) Chem Mater 14:4155
10. Kim C, Noh M, Choi M, Cho J, Park B (2005) Chem Mater 17:3297
11. Park M-S, Kang Y-M, Wang G-X, Dou S-X, Liu H-K (2008) Adv Funct Mater 18:455
12. Sharma Y, Sharma N, Subba Rao GV, Chowdari BVR (2008) Chem Mater 20:6829
13. Huang F, Yuan Z, Zhan H, Zhou Y, Sun J (2003) Mater Lett 57:3341
14. Courtney IA, Dahn JR (1997) J Electrochem Soc 144:2045
15. Li H, Huang X, Chen L (1999) Solid State Ionics 123:189
16. Uchiyama H, Hosono E, Honma I, Zhou H, Imai H (2008) Electrochem Commun 10:52
17. Wang X, Wen Z, Yang X, Lin B (2008) Solid State Ionics 179:1238
18. Yang J, Takeda Y, Imanishi N, Xie JY, Yamamoto O (2001) J Power Sources 97–98:216
19. Ning J, Dai Q, Jiang T, Men K, Liu D, Xiao N, Li C, Li D, Liu B, Zou B, Zou G, Yu WW (2009) Langmuir 25:1818
20. Chen MH, Huang ZC, Wu GT, Zhu GM, You JK, Lin ZG (2003) Mater Res Bull 38:831
21. Reddy MV, Subba Rao GV, Chowdari BVR (2008) In: Chowdari BVR et al (eds) 'Solid state ionics: New materials for pollution free energy devices' [Proceedings of the 11th Asian conf. on solid state ionics]. MacMillan, India, New Delhi, pp 187–193
22. Park C-M, Chang W-S, Jung H, Kim J-H, Sohn H-J (2009) Electrochem Commun 11:2165
23. Allimi BS, Alpay SP, Xie CK, Wells BO, Budnick JI, Pease DM (2008) Appl Phys Lett 92:202105
24. Grygiel C, Pautrat A, Rodière P (2009) Phys Rev B 79:235111
25. Rivadulla F, Rossier JF, Hernández MG, Quintela MAL, Rivas J, Goodenough JB (2007) Phys Rev B 76:205110
26. Das B, Reddy MV, Krishnamoorthi C, Tripathy S, Mahendiran R, Subba Rao GV, Chowdari BVR (2009) Electrochim Acta 54:3360
27. Das B, Reddy MV, Subba Rao GV, Chowdari BVR (2008) J Solid State Electrochem 12:953
28. Moreno MS, Punte G, Rigotti G, Mercader RC, Weisz AD, Blesa MA (2001) Solid State Ionics 144:81
29. Lee K-M, Lee Y-S, Kim Y-W, Sun Y-K, Lee S-M (2009) J Alloys Compd 472:461
30. Wachtler M, Besenhard JO, Winter M (2001) J Power Sources 94:189
31. Courtney IA, Tse JS, Mao O, Hafner J, Dahn JR (1998) Phys Rev B 58:15583
32. Park C-M, Sohn H-J (2009) Electrochim Acta 54:6367
33. Hassoun J, Derrien G, Panero S, Scrosati B (2008) Adv Mater 20:3169